nature communications

Article

https://doi.org/10.1038/s41467-025-57677-x

Contributions of biological and physical dynamics to deglacial CO_2 release from the polar Southern Ocean

Received: 25 November 2023

Accepted: 27 February 2025

Yuhao Dai [1,2] & **Jimin Yu** [1,3,4]

As a critical region regulating air-sea gas exchanges, the polar Southern Ocean has important implications for deglacial atmospheric CO_2 rises. However, proxy data evidence is sparse to evaluate the respective roles of Southern Ocean biological and physical dynamics in affecting past air-sea CO_2 exchanges due to longstanding challenges in obtaining carbonate materials to reconstruct surface conditions in this region. Here, we circumvent these challenges by constraining polar Southern Ocean surface-water conditions based on preformed deep-water properties derived from paired carbonate ion-phosphate-oxygenation reconstructions during the last deglaciation. We show that polar Southern Ocean carbon losses coincided with increased deep-ocean preformed nutrient concentrations, highlighting reduced biological carbon utilization as a key process for deglacial CO_2 outgassing. By comparing total carbon losses with those attributable to biological processes, we further show that enhanced physically-driven air-sea gas exchanges in the polar Southern Ocean strongly drove CO_2 outgassing towards the end of the last deglaciation.

Ice core measurements show rapid atmospheric CO_2 increases during the Late Pleistocene glacial-interglacial transitions[1–3]. These deglacial atmospheric CO_2 increases are thought to be linked to strengthened release of carbon previously stored in the deep ocean through the Polar Antarctic Zone (PAZ)[4–6]. Climate models suggest that changes in the PAZ enhanced the release of carbon previously sequestered via both biological and physical processes and thus raised atmospheric CO_2 during deglaciations[7–13]. However, mechanisms controlling past atmospheric CO_2 fluctuations remain elusive due to the lack of paleoclimate proxy records in the PAZ. This presents as an obstacle to confidently link PAZ processes to changes in deep-ocean carbon storage and atmospheric CO_2. Given the critical role of the Southern Ocean in governing atmospheric CO_2 on various timescales in the past and future[4,14,15], it is imperative to fully evaluate the respective roles of PAZ biological and physical processes in affecting atmospheric CO_2 using marine paleoclimate archives. Nevertheless, a longstanding challenge to investigate the PAZ is the difficulty to obtain sufficient carbonate materials for paleoclimate reconstructions.

Here, we circumvent this challenge by constraining PAZ conditions using two quasi-conservative properties of deep waters[7,15,16]: PO_4^* (refs. 16–18) and air-sea exchange signature of carbonate ion concentration ($[CO_3^{2-}]_{as}$)[19–22]. Following deep water formation, signatures of surface source waters can be preserved as "preformed" properties that are quasi-conservative in the ocean interior. PO_4^*, derived from concentrations of phosphate and oxygen ($[PO_4^{3-}]$ and $[O_2]$, respectively), has long been employed to infer the biological nutrient utilization efficiency and surface-water oxygen saturation in deep-water formation regions (Methods)[16–18]. PO_4^* is quasi-conservative because phosphate regeneration is stoichiometrically linked to oxygen consumption during biogenic matter decomposition in the ocean interior. For a given water mass, higher PO_4^* largely indicates less efficient nutrient utilization[7,16,17,23]. Recently, $[CO_3^{2-}]_{as}$ has been developed to

---

[1] Research School of Earth Sciences, Australian National University, Canberra, ACT, Australia. [2] Australian Centre for Excellence in Antarctic Science, Australian National University, Canberra, ACT, Australia. [3] Laoshan Laboratory, Qingdao, China. [4] SKLLQG, Institute of Earth Environment, Chinese Academy of Sciences, Xi'an, China. e-mail: yuhao.dai@anu.edu.au; jiminyuanu@gmail.com

constrain CO_2 exchanges between surface waters and the atmosphere[19–22]. $[CO_3^{2-}]_{as}$ is quasi-conservative in the ocean interior and represents changes in seawater carbonate ion concentration ($[CO_3^{2-}]$) due to the net air-sea CO_2 exchange when source waters leave the surface ocean, after correcting for anthropogenic carbon influences[19,20]. In addition to air-sea CO_2 exchanges in source-water regions, the distribution of deep-water $[CO_3^{2-}]$ is driven by changes in physical conditions in the ocean (salinity, temperature, and pressure), remineralization of sinking organic matter, and dissolution of carbonate. To reveal the effect of air-sea exchanges on $[CO_3^{2-}]$, calculation of $[CO_3^{2-}]_{as}$ accounts for $[CO_3^{2-}]$ changes driven by (1) physical conditions, (2) redistributions of dissolved inorganic carbon (DIC) and alkalinity related to regeneration of biogenic organic matter and carbonate, which can be estimated by $[PO_4^{3-}]$ variations, and (3) when considering temporal evolutions, global ocean DIC and alkalinity changes due to imbalances between riverine inputs and marine carbonate burial (Methods). Higher deep-water $[CO_3^{2-}]_{as}$ values reflect more net CO_2 losses through air-sea gas exchanges in source regions of the deep water[19,20].

Seawater PO_4^* and $[CO_3^{2-}]_{as}$ in the deep ocean is largely determined by mixing between southern sourced waters (SSWs) formed in the Southern Ocean and northern sourced waters (NSWs) formed in the North Atlantic (Fig. 1). In the preindustrial ocean, SSWs have higher PO_4^* than NSWs, reflecting less efficient nutrient utilization in the Southern Ocean[7,16,17]. Preindustrial SSWs have higher $[CO_3^{2-}]_{as}$ than NSWs because CO_2 tends to be released in the PAZ due to upwelling of high-DIC deep waters and inefficient biological utilization of nutrients and carbon[4,15,22]. Consequently, SSWs are less efficient to sequester atmospheric CO_2 than NSWs[19]. Given known water-mass mixing proportions, PO_4^* and $[CO_3^{2-}]_{as}$ reconstructed in the deep ocean away from polar regions can be used to infer water-mass endmember compositions and thereby surface conditions in deep-water formation regions. By contrast, nonconservative tracers such as $[PO_4^{3-}]$, $[CO_3^{2-}]$, and $[O_2]$ can vary substantially due to organic matter respiration within the ocean interior. The advantage of using PO_4^* and $[CO_3^{2-}]_{as}$ is illustrated by preindustrial ocean hydrography. For example, deep waters in the Pacific show large meridional gradients in $[PO_4^{3-}]$, $[CO_3^{2-}]$, and $[O_2]$, largely due to biogenic matter respiration on their northward transport route (Fig. 1 and Supplementary Fig. 1). By contrast, PO_4^* and $[CO_3^{2-}]_{as}$ in this ocean basin display nearly stable values, reflecting mixing of NSWs and SSWs at relatively fixed proportions (Fig. 1 and Supplementary Fig. 1).

It is worth noting that PO_4^* and $[CO_3^{2-}]_{as}$ are related to different aspects of the marine carbon cycle. While biologically-driven air-sea CO_2 exchange would be accompanied by PO_4^* changes, purely physically-driven CO_2 outgassing is largely independent of PO_4^*. Seawater $[CO_3^{2-}]_{as}$ changes are not tied to any specific mechanisms but they integrate net CO_2 air-sea exchange effects from both biological and physical processes. Therefore, combinational use of PO_4^* and $[CO_3^{2-}]_{as}$ may allow for distinguishing the respective roles of biological and physical processes in controlling atmospheric CO_2 changes.

In this study, we reconstruct deep-water PO_4^* and $[CO_3^{2-}]_{as}$ during the last deglaciation (18.0–11.7 ka) using sediment core MD97-2106 (45.15°S, 146.28°E, 3310 m water depth) from the Southwest Pacific (Fig. 1). Based on previous work[23], deep waters at site MD97-2106 are composed of about 30% NSWs and 70% SSWs in the preindustrial

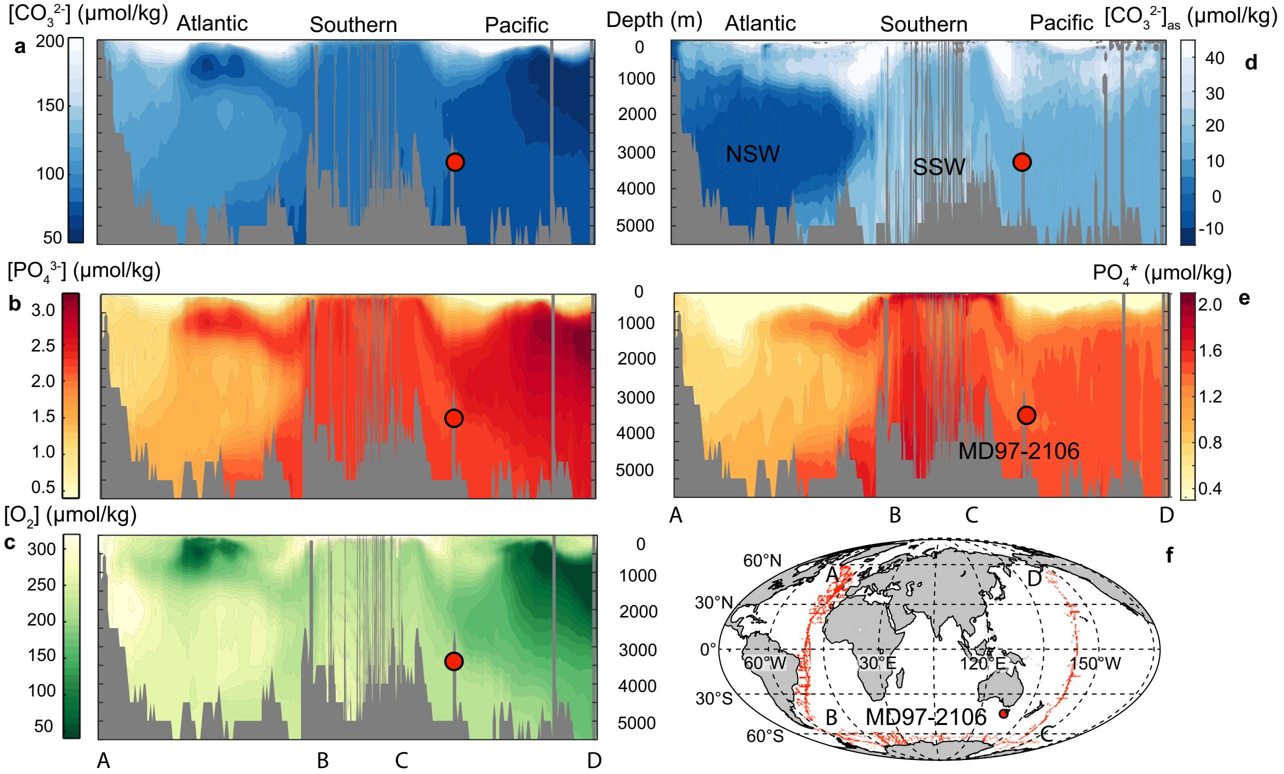

Fig. 1 | Preindustrial ocean biogeochemical properties. a $[CO_3^{2-}]$; (**b**), $[PO_4^{3-}]$; (**c**), $[O_2]$; (**d**), $[CO_3^{2-}]_{as}$; (**e**), PO_4^*; (**f**), Hydrographic sites used to generate transect profiles in (**a**–**e**) where the B-C distance is scaled down to better show meridional spans of the Atlantic (A-B) and Pacific (C-D). Note different colour shading scales in **a** and **d**, and in **b** and **e**. Red circles in (**a**–**f**) show the location of site MD97-2106. Data from GLODAPv2[61,62] are used to generate these transect profiles. Preindustrial DIC, derived by removing the anthropogenic component carbon from the total DIC[61,62], are used to calculate $[CO_3^{2-}]$ and $[CO_3^{2-}]_{as}$. Deep-water $[CO_3^{2-}]$, $[PO_4^{3-}]$, and $[O_2]$ (**a**–**c**) are non-conservative and affected by biogenic matter respiration, which would complicate inferring source water conditions base on these properties. By contrast, $[CO_3^{2-}]_{as}$ and PO_4^* in the ocean interior (**d**, **e**) are quasi-conservative[16,17,19–22], largely determined by the endmember values of northern sourced waters (NSWs), southern sourced waters (SSWs), and their mixing proportions (see Supplementary Fig. 1 for more details).

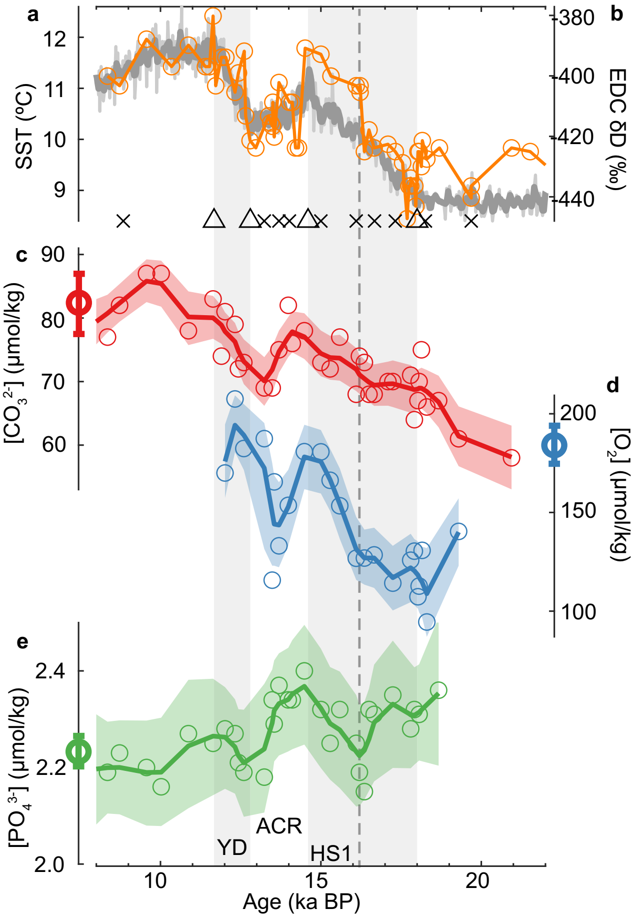

Fig. 2 | Deglacial reconstructions at site MD97-2106. a Sea surface temperature (SST)[28]. **b** EPICA Dome C (EDC) δD, a proxy for Antarctic temperature[72]. Triangles at the bottom are age tie points based on SST at site MD97-2106 and EDC δD, and crosses represent ^{14}C dates[28,29]. **c** Deep-water $[CO_3^{2-}]$; (**d**) Deep-water $[O_2]$; (**e**) Deep-water $[PO_4^{3-}]$. In (**c**–**e**) curves show LOESS smoothed probability maximum trends with envelopes representing ±1σ error ranges including uncertainties from analytical measurements, calibrations, and the age model. In (**c**–**e**), empty circles with error bars on the *y*-axes show the averages and ±1 standard deviations for the late Holocene data derived from core-top sediment samples. Grey vertical shadings highlight the Younger Dryas (YD) and Heinrich Stadial 1 (HS1), which are interrupted by the Antarctic Cold Reversal (ACR). The vertical dashed line marks the boundary between the early and late stages of HS1.

ocean (Methods). Due to the dominant influence from SSWs, our core is ideal to constrain preformed conditions of the PAZ surface waters, albeit possible past changes in NSW-SSW mixing ratio must also be considered. We reconstruct deep-water $[CO_3^{2-}]$ from B/Ca in benthic foraminifera[24], $[PO_4^{3-}]$ from Cd/Ca in benthic foraminifera[25,26], and $[O_2]$ from the carbon isotope gradient between epifaunal and deep infaunal benthic foraminifera[27] (Fig. 2 and Supplementary Fig. 2; Methods). Deep-water PO_4* is derived from $[PO_4^{3-}]$ and $[O_2]$ (refs. 16,17), and $[CO_3^{2-}]_{as}$ is calculated using $[CO_3^{2-}]$, $[PO_4^{3-}]$, physical conditions, and modelled global alkalinity changes[19] (Fig. 3; Methods). These two preformed tracers were derived only when underlying proxy reconstructions were available from the same sediment depths. The fully propagated average uncertainties of PO_4* and $[CO_3^{2-}]_{as}$ are 0.15 and 7.7 μmol/kg (1σ), respectively, and uncertainties on derived properties are given at 1σ throughout this work. The chronology of our core during the last deglaciation is constrained by 8 planktic radiocarbon dates and 4 age tie-points to Antarctic temperature as previously reported[28,29] (Fig. 2a and Supplementary Fig. 3). See Methods for reconstruction details.

Results

Increased PAZ air-sea CO_2 sequestration at the Last Glacial Maximum

Figure 2 shows reconstructed deep-water $[PO_4^{3-}]$, $[O_2]$, and $[CO_3^{2-}]$ during the last deglaciation and their late Holocene (LH; 4.2–0 ka) averages (Supplementary Data 1). From the Last Glacial Maximum (LGM; 18–22 ka) to the LH, our reconstructions show that deep-water $[PO_4^{3-}]$ declined by 0.10±0.04 μmol/kg (aggregated 1 standard deviation of two compared periods), and $[O_2]$ increased by 75±21 μmol/kg, which is similar to previous records[30] (Supplementary Fig. 4). Combining $[PO_4^{3-}]$ and $[O_2]$, the calculated PO_4* shows an increase by 0.3±0.1 μmol/kg from the LGM to the LH (Fig. 2). During the same time interval, deep-water $[CO_3^{2-}]$ at our site increased by 16±6 μmol/kg (Fig. 2). In the absence of CO_2 exchanges, warmer temperature, lower salinity, and deeper water depth together would lower $[CO_3^{2-}]$ at our site by ~2 μmol/kg during the LH compared to the LGM (Fig. 3). Also, assuming no CO_2 exchanges, DIC and alkalinity decreases caused by regeneration of biogenic organic matter and carbonate that are linked to the $[PO_4^{3-}]$ decrease of 0.10±0.04 μmol/kg would raise $[CO_3^{2-}]$ by 5±2 μmol/kg from the LGM to the LH (Fig. 3). Global ocean DIC and alkalinity declines associated with $CaCO_3$ input/output imbalances would lower $[CO_3^{2-}]$ by 26 μmol/kg (Fig. 3). Because the magnitude of the global alkalinity change cannot yet be reconstructed by proxies, we here rely on model simulations to calculate its effect on $[CO_3^{2-}]_{as}$[31]. However, different choices of modelled deglacial glacial alkalinity change only marginally affects the structure of the deglacial $[CO_3^{2-}]_{as}$ changes (Supplementary Fig. 5). The offset between the reconstructed $[CO_3^{2-}]$ change and the expected $[CO_3^{2-}]$ changes without air-sea CO_2 exchange is attributed to air-sea CO_2 exchange signals, that is, $[CO_3^{2-}]_{as}$. Based on our calculations, we derive an LGM-to-LH $[CO_3^{2-}]_{as}$ increase of 39±6 μmol/kg. Past changes in stoichiometry compositions of remineralized biogenic matter would introduce uncertainties in our calculated PO_4* and $[CO_3^{2-}]_{as}$, but they minimally affect our conclusion as shown by sensitivity tests (Supplementary Figs. 5, 6).

To infer LGM SSW PO_4* and $[CO_3^{2-}]_{as}$ from reconstructions at site MD97-2106, SSW-NSW mixing ratios (represented by SSW% and NSW% hereafter; SSW% + NSW% = 100%) at our site and the LGM NSW endmember values need to be constrained. In the preindustrial ocean, SSW% at site MD97-2106 is about 70%, based on PO_4*of 1.36 μmol/kg at our site with SSW and NSW PO_4* endmember values being 1.64±0.06 and 0.73±0.06 μmol/kg, respectively (Fig. 4; Table 1). The preindustrial $[CO_3^{2-}]_{as}$ of 6.7 μmol/kg at our site is consistent with 70% SSWs with $[CO_3^{2-}]_{as}$ of 10±3 μmol/kg and 30% NSWs with $[CO_3^{2-}]_{as}$ of -17±5 μmol/kg (Fig. 4, Table 1). During the LGM, SSW% in the deep South Pacific was higher than the LH as indicated by neodymium isotopes (ε_{Nd}) records[32,33], due to shoaling of the upper limb of the global overturning circulation[15,34–36]. We thus assume the LGM SSW% at our site to be 80%. LGM NSW PO_4* has not been reconstructed based on proxies but is expected to be less variable than the LGM SSW PO_4* (refs. 7,8,15,37). We assume the LGM NSW PO_4* to be 0.58±0.06 μmol/kg, which is 80% of the modern level, following ref. 37. LGM NSW $[CO_3^{2-}]_{as}$ is inferred to be -43±5 μmol/kg from a reconstruction in the North Atlantic (Supplementary Fig. 7). Considering the above SSW% and NSW endmember values along with our reconstructions at site MD97-2106, the LGM PO_4* and $[CO_3^{2-}]_{as}$ of SSWs are estimated to be 1.18±0.13 and -34±10 μmol/kg, respectively (Table 1). Additional sensitivity tests show that uncertainties associated with SSW% and NSW endmembers only marginally affect our final SSW PO_4* and $[CO_3^{2-}]_{as}$ results during the LGM (Supplementary Fig. 8). We find that LGM SSW PO_4* and $[CO_3^{2-}]_{as}$ were lower than their LH levels (Fig. 4), suggesting enhanced carbon sequestration in the PAZ during the LGM.

The reduced LGM SSW PO_4* compared to the LH could be driven by lower preformed $[PO_4^{3-}]$ and/or lower preformed $[O_2]$. Lower LGM preformed $[PO_4^{3-}]$ would indicate declines in surface-water phosphate and associated DIC in the PAZ[7,8] that were driven by biological processes. For lower LGM preformed [O_2], insufficient O_2 air-sea exchange imposed by physical barriers such as sea ice that would retain O_2 deficiencies of upwelled-and-then-downwelled waters in the PAZ[38]. However, purely physically-driven component of the lowered PAZ preformed [O_2] is deemed to be relatively small between LGM and LH based on model simulations[38]. Therefore, declines in PAZ preformed [O_2] must largely originate from previous organic matter remineralization that consumed O_2 and produced CO_2 in tandem. Such a biologically-driven PAZ preformed [O_2] decline must be accompanied by surplus CO_2 that is retained in the newly formed deep waters, because of the longer air-sea exchange equilibration time of CO_2 than O_2 (refs. 39,40). Therefore, lowered LGM SSW PO_4^*, regardless of relative contributions of preformed [PO_4^{3-}] and preformed [O_2], is stoichiometrically linked to an more DIC sequestered by biological processes in the PAZ. If completely driven by more efficient nutrient utilization, an LGM-LH change in SSW PO_4^* of 0.46±0.14 μmol/kg would be associated with a DIC decrease of 58±18 μmol/kg due to enhanced biological CO_2 uptake in the PAZ during the LGM. Such a change in biologically-driven DIC uptake may be slightly overestimated due to a potential but minor contribution of physically-driven disequilibrium to the lowered LGM SSW PO_4^*. Our LGM PO_4^* reconstruction shows that more phosphate and DIC supplied from the subsurface was biologically utilized in the PAZ, despite lower glacial export productivities in the region[6,41]. The associated biological processes would draw down surface-water CO_2 partial pressure, with an effect to strengthen carbon sequestration in the ocean by a maximum amount of 58±18 μmol/kg.

Our SSW PO_4^* reconstruction provides new evidence for increased carbon uptake during the LGM caused by more efficient nutrient utilization in the surface Southern Ocean as revealed by published nitrogen isotope ($\delta^{15}N$) records[42–45]. Importantly, our PO_4^* reconstruction reflects an integrated influence of biological processes on the Southern Ocean biogeochemistry and thus can complement surface-ocean $\delta^{15}N$ records, which are presumably biased towards spring-summer seasonality of phytoplankton blooms that are offset from wintertime deep water formation. Moreover, our PO_4^* reconstruction demonstrates that reduced preformed nutrient concentrations in the PAZ, driven by more complete utilization of nutrient and carbon supplied to the surface Southern Ocean in spite of lowered export productivity[6,41,45], was propagated downstream to great water depths during the LGM. Our PO_4^* reconstructions thus lend strong support for an enhanced biological pump in the PAZ to lower atmospheric CO_2 during the LGM[5,7,8,15].

Lower LGM SSW [CO_3^{2-}]$_{as}$ also more directly demonstrates that atmospheric CO_2 was more efficiently sequestered via the PAZ. The sensitivity of [CO_3^{2-}]$_{as}$ change to DIC change is previously shown to depend on [CO_3^{2-}]$_{as}$ (ref. 19) and is estimated to be -0.4 on average over the range of [CO_3^{2-}]$_{as}$ values reconstructed at our site[19]. Based on this sensitivity, the reconstructed LGM-LH change in SSW [CO_3^{2-}]$_{as}$ change (-44±10 μmol/kg) corresponds to 110±25 μmol/kg more CO_2 sequestration in the PAZ during the LGM that includes CO_2 sequestration caused by both biological and physical processes. This carbon sequestration during the LGM in the PAZ derived from [CO_3^{2-}]$_{as}$, although dependent on the global alkalinity derived from model simulations, is larger than the upper limit of the biologically-driven air-sea CO_2 uptake of 58±18 μmol/kg estimated from PO_4^*. The large difference between CO_2 uptake changes based on [CO_3^{2-}]$_{as}$ and PO_4^* suggests that in addition to biological processes, physical dynamics such as fluctuations associated with sea-ice extent[10,11], Southern Ocean overturning circulation[34,43], and southern hemisphere westerlies[44,46,47] are an essential contributor to enhanced carbon sequestered in the PAZ during the LGM.

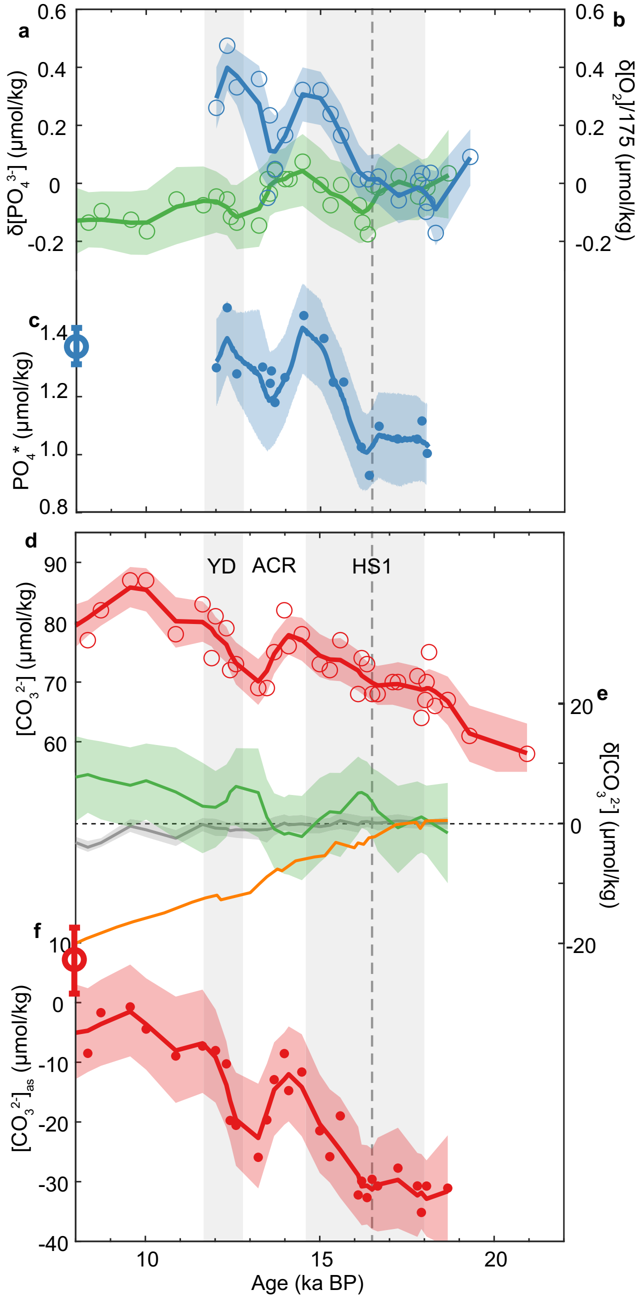

Fig. 3 | Deriving PO_4^* and [CO_3^{2-}]$_{as}$ at site MD97-2106. Upper panel shows changes in [PO_4^{3-}] (**a**) and [O_2]/175 (**b**) relative to the LGM averages. PO_4^* (**c**) is determined by the sum of [PO_4^{3-}] and [O_2]/175. Lower panel shows reconstructed [CO_3^{2-}] (**d**) alongside expected changes in [CO_3^{2-}] relative to the LGM values (**e**), due to temperature-salinity-pressure variations (grey curve), DIC-alkalinity redistributions linked to [PO_4^{3-}] variations (green curve), and temporal global ocean alkalinity-DIC changes linked to $CaCO_3$ input/output imbalance (orange curve). All curves shown in (**e**) assume no air-sea CO_2 exchange. **f** calculated [CO_3^{2-}]$_{as}$. In (**c**–**f**) empty circles with error bars on the y-axes show the averages and ±1 standard deviations for the late Holocene data. Envelopes associated with curves represent ±1σ error ranges incorporating uncertainties from analytical measurements, calibrations, and the age model. The deglacial PO_4^* pattern is dominantly driven by [O_2] changes, while millennial-timescale [CO_3^{2-}]$_{as}$ variabilities are mainly driven by changes in [CO_3^{2-}] with secondary contributions from DIC-alkalinity variations linked to [PO_4^{3-}] fluctuations. Grey vertical shadings highlight the Younger Dryas (YD) and Heinrich Stadial 1 (HS1), which are interrupted by the Antarctic Cold Reversal (ACR). The vertical dashed line marks the boundary between the early and late stages of HS1.

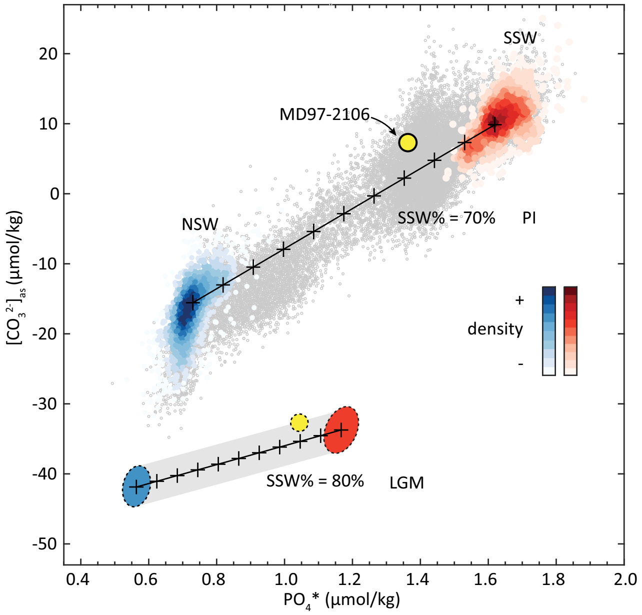

Fig. 4 | Mixing between northern and southern sourced waters during the preindustrial era (PI) and the Last Glacial Maximum (LGM). PI data are hydrographic data from the GLODAPv2 dataset with anthropogenic carbon deducted[61,62]. Hydrographic data defining northern sourced water (NSW) and southern sourced waters (SSW) endmembers are shown by blue and red circles, respectively, with darker colour emphasizing higher distribution density. Grey dots are hydrographic data from global ocean deeper than 2 km (excluding the Arctic Ocean). The black line is the NSW-SSW mixing curve. The yellow circle indicates PO_4^* and $[CO_3^{2-}]_{as}$ reconstructions derived from late Holocene sediment samples at site MD97-2106, which are consistent with the hydrographic data. LGM data are shown by circles with dashed edges. During the LGM, PO_4^* and $[CO_3^{2-}]_{as}$ reconstructed at site MD97-2016, together with NSW endmember values, are used to deduce SSW endmember values, assuming 80% of glacial SSWs at our site. Any increase of SSW% at MD97-2106 would lower SSW endmember $[CO_3^{2-}]_{as}$ and PO_4^* values. For the LGM ocean, sizes of the endmember circles indicate the ±1σ variabilities of PO_4^* and $[CO_3^{2-}]_{as}$.

Biologically driven PAZ CO_2 outgassing during Heinrich Stadial 1

High sedimentation rates and tightly constrained chronology in our core allow us to generate detailed deglacial reconstructions (Fig. 5; Methods). During Heinrich Stadial 1 (HS1; 18.0–14.6 ka), PO_4^* at our site remained stable during the first 2 ka and rapidly increased by 0.4±0.1 μmol/kg towards the end of HS1 (Fig. 5d). $[CO_3^{2-}]_{as}$ at our site displayed a similar pattern, showing minimal change during early HS1 and an increase of 19±3 mol/kg during late HS1 (Fig. 5c). During HS1, SSW% at our site likely increased due to substantially decreased NSW production as indicated by proxy data[48] (Fig. 5b). Everything else being equal, an SSW% increase from an LGM level of 80% to the extreme but unlikely level of 100% would raise PO_4^* and $[CO_3^{2-}]_{as}$ at our site by 0.11 and 5 μmol/kg, respectively. Any deglacial NSW PO_4^* increase likely occurred after HS1, making little contribution to the reconstructed PO_4^* change at our site during HS1[49]. NSW $[CO_3^{2-}]_{as}$ increased by 7 μmol/kg as shown by previous reconstructions[20] (Supplementary Fig. 7), which could raise $[CO_3^{2-}]_{as}$ by at most 2 μmol/kg at site MD97-2106 assuming no SSW% increase (a condition that maximizes the NSW-endmember influence at our site). Therefore, we conclude that PO_4^* and $[CO_3^{2-}]_{as}$ increases observed at our site during HS1 can be largely attributed to changes in the SSW endmember values.

During early HS1, both PO_4^* and $[CO_3^{2-}]_{as}$ remained invariant at our site, suggesting that changes in air-sea CO_2 sequestration in the PAZ were too small to be resolved beyond our reconstruction uncertainties. The roughly stable SSW PO_4^* during early HS1 coincided with minor nutrient utilization changes shown by opal flux[41] and $\delta^{15}N$ records[42–45] in the Open Antarctic Zone (OAZ) (Supplementary Fig. 9), the latter of which is well dated in deep-sea coral samples (Fig. 5f). Thus, our new and literature data suggest that PAZ biological processes changed little during early HS1. Nearly constant early-HS1 SSW $[CO_3^{2-}]_{as}$ further suggests little changes in air-sea CO_2 exchanges in the PAZ during this period, including those may be caused by physical processes. This seems to contradict with other proxy records, which indicate favourable physical conditions for CO_2 outgassing during early HS1. During this period, Antarctic ice-core sea-salt sodium concentrations suggest Southern Ocean sea-ice extent possibly retreated[46], and sediment core radiocarbon data indicate improved deep Southern Ocean ventilation at multiple locations including our site[28,30,50]. According to model simulations[9,51], enhanced deep Southern Ocean radiocarbon ventilation might be partially driven by changing geometry of the global overturning circulation that is strongly modulated by the sea-ice extent[34]. Although retreating sea ice itself would promote air-sea gas exchange, the lack of strong CO_2 outgassing resolvable by our $[CO_3^{2-}]_{as}$ reconstruction might be related to minor warming in the PAZ and deep Southern Ocean during early HS1[52], which has been shown by model simulations to be crucial to modulate physically-driven CO_2 outgassing[9,13]. Nevertheless, further investigations are needed to better understand how physically-driven air-sea exchanges in the PAZ affected deep-ocean radiocarbon and carbon storage during early HS1.

During late HS1, increased PO_4^* suggests more biologically unutilized nutrients relative to the supply and thus a weaker biological pump in the PAZ. This is corroborated by $\delta^{15}N$ records in the OAZ[42–45] (Fig. 5f and Supplementary Fig. 9), which show prominent decreases in nutrient utilization efficiency over the same period. Ignoring the minor contribution of purely physically driven preformed $[O_2]$ to PO_4^*, PO_4^* that was raised by 0.4±0.1 μmol/kg at our site suggests 44±10 μmol/kg of DIC became unutilized by biological processes during late HS1. Rising SSW $[CO_3^{2-}]_{as}$ during late HS1 also suggests that CO_2 released through air-sea exchange in the PAZ during this period (Fig. 5c). Based on the $[CO_3^{2-}]_{as}$ increase of 19±3 mol/kg, 46±11 μmol/kg DIC was released from deep waters at site MD97-2106 during late HS1. Comparable DIC changes estimated based on PO_4^* and $[CO_3^{2-}]_{as}$ demonstrate that increased DIC related to biologically unutilized nutrients can largely account for CO_2 outgassing in the PAZ during late HS1. Physical processes must have facilitated outgassing of these biology-related DIC during late HS1. For example, given the rising export productivity in the OAZ during this period[41] (Fig. 5g), declines in deglacial nutrient utilization efficiency during HS1 must be driven by more nutrient supplied by enhanced deep water upwelling[5,15,41]. However, direct contribution of physical processes to promoting CO_2 outgassing independent of biological processes appears to be small during late HS1.

Reduced PAZ CO_2 outgassing during the Antarctic Cold Reversal

During the Antarctic Cold Reversal (ACR; 14.6–12.8 ka), PO_4^* and $[CO_3^{2-}]_{as}$ declined at site MD97-2106 by 0.22±0.08 and 11±5 μmol/kg, respectively (Fig. 5). During this period, reinvigorated production of low-PO_4^* and low-$[CO_3^{2-}]_{as}$ NSWs[48] would reduce SSW% and thereby lower PO_4^* and $[CO_3^{2-}]_{as}$ at our site (Figs. 1, 4 and Supplementary Fig. 1). Without changes in NSW and SSW endmember values, the reconstructed PO_4^* and $[CO_3^{2-}]_{as}$ declines could be largely explained by 30% reduction in SSW% from 100% (highest possible HS1 level) to 70% (ACR level). However, this would require no NSWs at our site during HS1 that is inconsistent with deep Southern Ocean ε_{Nd} records[32,33]. A large SSW% reduction would also raise $[O_2]$ during the ACR, opposite to the reconstructed trends at our site (Fig. 2d) and the Drake Passage[53]. Therefore, SSW% decline is inadequate to explain all the reconstructed PO_4^* and $[CO_3^{2-}]_{as}$ changes at our site. A moderate SSW% decline by 15% from HS1 would lower PO_4^* and $[CO_3^{2-}]_{as}$, respectively, by 0.12 and 4 μmol/kg, which are too small to account for our reconstructed changes. Hence, we

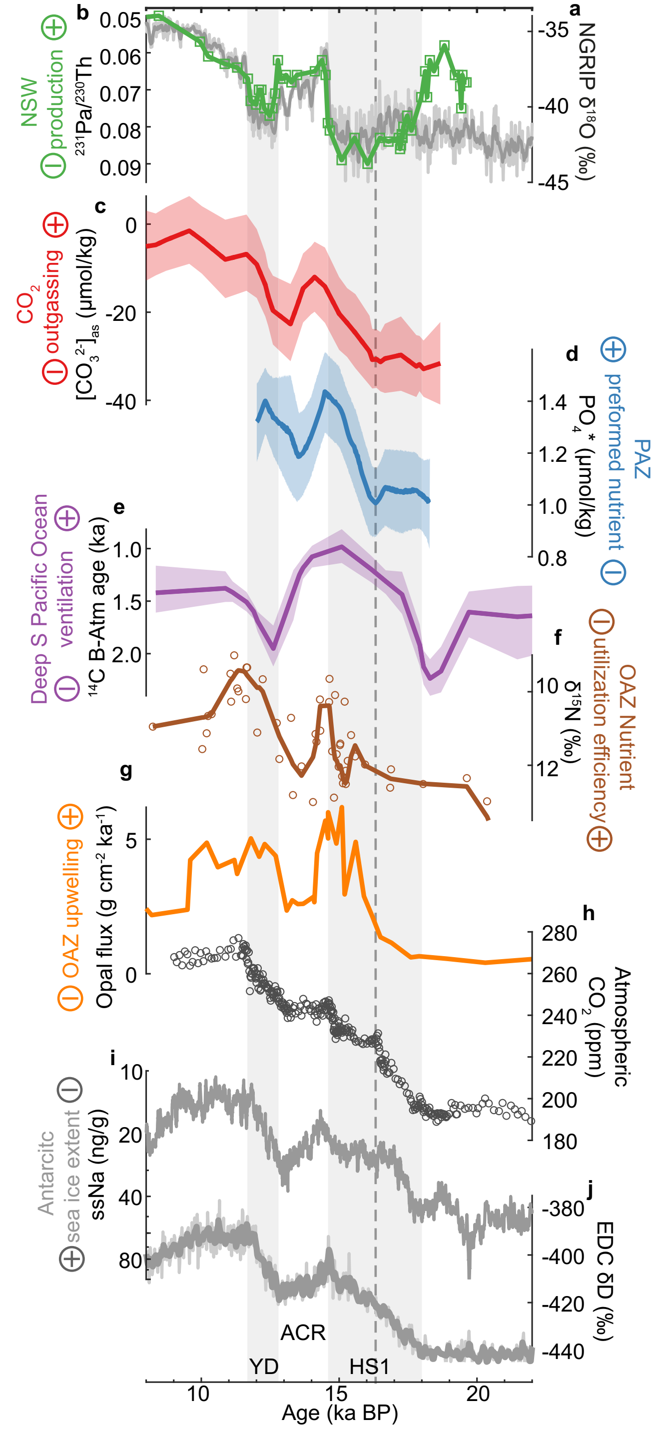

Fig. 5 | Deglacial records indicating deep South Pacific carbon losses. **a** Greenland NGRIP ice-core δ^{18}O (ref. 73). **b** Northern sourced water (NSW) production strength indicated by ^{231}Pa/^{230}Th in the North Atlantic[48]. **c** MD97-2106 [CO$_3^{2-}$]$_{as}$. **d** Deep-water PO$_4$* at MD97-2106, largely reflecting preformed nutrient concentration in the Polar Antarctic Zone (PAZ). **e** ^{14}C ventilation ages at site MD97-2106[28]. **f** deep-sea coral-bound nitrogen isotopes from the Drake Passage reflecting nutrient utilization efficiency in the Open Antarctic Zone (OAZ)[42,43]. **g** Opal flux from the Atlantic-Sector Southern Ocean indicating the OAZ upwelling strength[41]. **h** Ice-core atmospheric CO$_2$[2]. **i**, Ice-core sea-salt sodium concentrations, a proxy for the Southern Ocean sea-ice extent[46]. Note the log scale of *y*-axis. **j** EDC ice δD, a proxy for Antarctic temperature[72]. In (**c**–**e**) Envelopes associated with curves represent ±1σ error ranges incorporating uncertainties from analytical measurements, proxy calibrations, and the age model. Grey vertical shadings highlight the Younger Dryas (YD) and Heinrich Stadial 1 (HS1), which are interrupted by the Antarctic Cold Reversal (ACR). The vertical dashed line marks the boundary between the early and late stages of HS1.

conclude that SSW PO$_4$* and [CO$_3^{2-}$]$_{as}$ endmember values likely decreased during the ACR.

Our inferred SSW PO$_4$* reduction suggests a decrease in the preformed nutrient and DIC due to more efficient nutrient utilization in the PAZ during the ACR, in line with OAZ δ^{15}N records[41–45] and enhanced marine productivity deduced from marine-derived aerosols recorded by ice cores[54]. The biologically-driven air-sea CO$_2$ sequestration is also registered by the reconstructed [CO$_3^{2-}$]$_{as}$ decline (Fig. 5c). In addition to biological changes, the enhanced CO$_2$ sequestration may be linked to physical processes including readvancing Antarctic sea ice[46] that limited air-sea gas exchange and northward shift of the Southern Hemisphere westerlies[44,53]. We suggest that both biological and physical changes contributed to enhanced air-sea CO$_2$ sequestration during the ACR.

Strong physically driven PAZ CO$_2$ outgassing during the Younger Dryas

During the Younger Dryas (YD; 12.8–11.7 ka), deep-water PO$_4$* and [CO$_3^{2-}$]$_{as}$ increased by 0.10±0.11 μmol/kg and 16±5 μmol/kg at our site, respectively (Fig. 5c, d). Proxy data suggest that SSW% in the deep Southern Ocean during the YD declined towards the Holocene level[32,35]. Any decline in SSW% tends to lower PO$_4$*, opposite to the reconstructed increasing PO$_4$* at our site. The NSW PO$_4$* possibly increased by ~0.15 μmol/kg during the YD[49], with an effect of raising PO$_4$* by 0.04 μmol/kg, assuming Holocene SSW% level of 70% at our site (a condition that maximizes the impact of NSW endmember changes). The remaining PO$_4$* increase of 0.06±0.11 μmol/kg at our site must be due to an increase in SSW endmember PO$_4$*. We estimate that SSW PO$_4$* was increased by 0.08±0.17 μmol/kg with SSW% level of 70% at our site. For [CO$_3^{2-}$]$_{as}$, an NSW endmember [CO$_3^{2-}$]$_{as}$ increase of 15±7 μmol/kg (Supplementary Fig. 7) could account for at most 5±2 μmol/kg [CO$_3^{2-}$]$_{as}$ increase at site MD97-2106, assuming an SSW% of 70%. The remaining 11±6 μmol/kg increase in [CO$_3^{2-}$]$_{as}$ at our site must be caused by an SSW endmember [CO$_3^{2-}$]$_{as}$ increase of 16±9 μmol/kg. Therefore, both PO$_4$* and [CO$_3^{2-}$]$_{as}$ increases at MD97-2106 are strongly driven by increases in their SSW endmember values during the YD.

Our inferred SSW PO$_4$* increase during the YD agrees with OAZ δ^{15}N records[41–45], indicative of lowered nutrient utilization efficiency in the OAZ. The 0.08±0.17 μmol/kg increase in SSW PO$_4$* suggests 8±18 μmol/kg increase in DIC, which could cause a maximum magnitude of 8±18 μmol/kg CO$_2$ outgassing, due to biological changes in the PAZ during the YD. Meanwhile, the 16±9 μmol/kg increase SSW [CO$_3^{2-}$]$_{as}$ indicate a total air-sea CO$_2$ loss of 40±23 μmol/kg. Thus, the PAZ CO$_2$ outgassing during the YD must be mainly attributed to physical processes including substantial sea ice retreat[46], Southern Ocean circulation changes[43], and southward shift of Southern Hemisphere westerlies[44,46,47].

Discussion

Using paired reconstructions of deep-water biogeochemical variables in the deep Southern Ocean, we have derived quasi-conservative tracers, PO$_4$* and [CO$_3^{2-}$]$_{as}$, to quantify carbon cycle changes in the PAZ during the last deglaciation. Our reconstructions show that the partitioning of carbon between the deep Southern Ocean and the atmosphere via air-sea CO$_2$ exchanges in the PAZ were mediated by biological and physical processes both between the LGM and Holocene and on millennial timescales during the deglaciation. PAZ CO$_2$ outgassing is more strongly associated with biological processes

Table 1 | PO_4* and $[CO_3^{2-}]_{as}$ values of NSW, SSW, and at site MD97-2106 during the preindustrial era, the Late Holocene, and the Last Glacial Maximum

	NSW		SSW		MD97-2106		
	PO_4*	$[CO_3^{2-}]_{as}$	PO_4*	$[CO_3^{2-}]_{as}$	PO_4*	$[CO_3^{2-}]_{as}$	SSW%
	µmol/kg	µmol/kg	µmol/kg	µmol/kg	µmol/kg	µmol/kg	
PI	0.73 ± 0.06	-17 ± 5	1.64 ± 0.06	10 ± 3	1.36	6.7	70%
LH					1.36 ± 0.05	6 ± 5	70%
LGM	0.58±0.06	-43 ± 5	1.18 ± 0.13	-34 ± 10	1.06 ± 0.08	-33 ± 3	80%

Preindustrial (PI) data are derived from hydrographic data[61]. Late Holocene (LH) data at site MD97-2106 are derived from core-top sediment samples. Last Glacial Maximum (LGM) SSW endmembers are estimated based on reconstructions at site MD97-2106, NSW endmembers from the literature[20,37], and an SSW% of 80% at site MD97-2106.

during HS1 and can be largely attributed to physical processes during the YD.

Our reconstructed variabilities in PAZ air-sea CO_2 exchanges are broadly consistent with deglacial atmospheric CO_2 changes[2], supporting the key role of the PAZ in regulating past atmospheric CO_2 (refs. 4–6). Nevertheless, our reconstructions also show that PAZ air-sea CO_2 exchanges at times deviated from atmospheric CO_2 fluctuations, implying complex mechanisms affecting deglacial atmospheric CO_2. For example, enhanced PAZ CO_2 outgassing during late HS1 diagnosed here appears to lag the atmospheric CO_2 rise that started from early HS1 (ref. 2). Also, our identified CO_2 outgassing reduction during the ACR coincided with an atmospheric CO_2 plateau[2]. These deviations between Southern Ocean outgassing and atmospheric CO_2 evolutions imply critical influences of other ocean volumes (e.g., upper oceans[29]) and/or regions (e.g., Atlantic sector of the Southern Ocean and the North Atlantic[20,55]) on past atmospheric CO_2 changes. Investigations of broader oceanic regions are warranted to better understand ocean-atmosphere carbon interactions, and quasi-conservative tracers such as PO_4* and $[CO_3^{2-}]_{as}$ employed here provide useful tools for future studies.

Methods

Trace element and stable isotope analyses

We examined sediment samples from 0–17 cm and 54–225 cm at site MD97-2106. For each sample, the >212 µm fractions of sediments were examined for benthic foraminifera *Cibicidoides wuellerstorfi* (sensu stricto)[56], *Hoeglundina elegans*, and *Globobulimina affinis*. *C. wuellerstorfi* can be continuously found throughout the section. *H. elegans* is abundant above 158 cm, but absent below 207 cm. *G. affinis* can be found below 96 cm, but is absent above this level, except in 0–17 cm of the core. For trace element analyses, 4–20 *C. wuellerstorfi* shells and 2–8 *H. elegans* shells were picked from each sample. When the number of *C. wuellerstorfi* shells was larger than 15 or the number of *H. elegans* was larger than 6, uncrushed shells were split into two subsamples and treated separately in further steps.

Foraminifera shells were first gently crushed between glass slides. *C. wuellerstorfi* shells were cleaned following the modified Mg-cleaning protocol[57,58] and *H. elegans* samples were cleaned following the Cd-cleaning protocol including the reductive step[59]. The cleaned samples were dissolved in 0.1 M HNO_3 and trace element-to-calcium ratios were measured on an ICP-MS at the Australian National University following the method of ref. 60. Analytical uncertainties (1 standard deviation) are >2% for B/Ca and Cd/Ca. Relative standard deviations of replicated *C. wuellerstorfi* B/Ca and *H. elegans* Cd/Ca are 1.5-2.6% (3 samples) and 1.0–3.1% (6 samples), respectively. These replicated subsamples are plotted separately in Supplementary Fig. 2.

For carbon and oxygen isotope analyses, 2–5 *C. wuellerstorfi* shells and 2–5 *G. affinis* shells were picked from each sample from the same sediment depths. The analyses were performed at the Institute of Earth Environment, Chinese Academy of Sciences. The precision is better than 0.08‰ for $\delta^{13}C$ and $\delta^{18}O$ analyses, based on repeated measurements of an in-house dolomite standard (TTB1).

Estimating seawater biogeochemistry

Modern hydrographic data near site MD97-2106 (temperature, salinity, DIC, alkalinity, silicate, phosphate, oxygen, and anthropogenic carbon) are retrieved from the GLODAPv2 gridded database[61,62]. The anthropogenic carbon is deducted from the measured DIC to obtain the preindustrial DIC levels. Carbonate chemistry parameters are calculated from hydrological data using CO2sys2.1[63].

Down-core in-situ deep-water $[CO_3^{2-}]$ ($[CO_3^{2-}]_{in-situ}$) is reconstructed from B/Ca in benthic foraminifera *C. wuellerstorfi*. $[CO_3^{2-}]_{in-situ}$ can be defined by calcite saturation state ($\Delta[CO_3^{2-}]$) and calcite saturation values ($[CO_3^{2-}]_{sat}$):

$$[CO_3^{2-}]_{in\ situ} = \Delta[CO_3^{2-}] + [CO_3^{2-}]_{sat}. \tag{1}$$

$\Delta[CO_3^{2-}]$ can be estimated *from C. wuellerstorfi* B/Ca using the calibration from Yu, et al.[64]:

$$B/Ca = (1.14 \pm 0.04)^{*}\Delta[CO_3^{2-}] + 176.6 \pm 1.0. \tag{2}$$

We adopt the modern $[CO_3^{2-}]_{sat}$ for the deglacial reconstruction, because $[CO_3^{2-}]_{sat}$ is insensitive to past temperature, salinity, and pressure changes which would only cause ~0.1 µmol/kg variations in $[CO_3^{2-}]_{sat}$ at Site MD97-2106 on glacial-interglacial timescales. We use a Monte-Carlo approach to combine the uncertainties in both proxy data and the age model. To combine these uncertainties, 10,000 iterations of the record were firstly randomly generated considering uncertainties associated with the B/Ca-$[CO_3^{2-}]$ calibration, B/Ca measurements, and the age model. Secondly, the 10,000 iterations were smoothed by a LOESS function. The 1σ uncertainty is defined as half of the difference between the 84th and 16th percentile of the smoothed curves. The combined ±1σ uncertainty of $[CO_3^{2-}]$ is, on average, ±4.5 µmol/kg for the range of B/Ca observed in core MD97-2106.

Past deep-water $[PO_4^{3-}]$ is derived from seawater Cd concentration (Cd_w) reconstructed from Cd/Ca in benthic foraminifera *H. elegans*. Cd_w is estimated by the following equation[65]:

$$Cd_w(nmol/kg) = [(Cd/Ca)_{foram}/D_{Cd}]^{*}10, \tag{3}$$

where D_{Cd} is the partition coefficient of Cd between foraminifera carbonate and seawater. For *H. elegans*, D_{Cd} is 1.0 and independent of water depth[25,66]. We apply 5% uncertainty to D_{Cd} when estimating the uncertainty of seawater $[PO_4^{3-}]$. Cd_w is used to estimate $[PO_4^{3-}]$ based on the relationship between Cd_w and $[PO_4^{3-}]$ for sites from the GEOTRACES transect GIPY06 located at the South of Tasmania[67]:

$$Cd_w = 1.23^{*}[PO_4^{3-}] + 1.30\ ([PO_4^{3-}] > 1.5\mu mol/kg, \\ r^2 = 0.76, n = 294, RMSE = 0.117). \tag{4}$$

Using different Cd_w-$[PO_4^{3-}]$ relations (e.g., a linear correlation for data from the entire GIPY06 transect and a quadratic relation based on the whole GEOTRACES dataset, 2021v2[68]) would result in different absolute $[PO_4^{3-}]$ values, but downcore $[PO_4^{3-}]$ patterns remain similar (Supplementary Fig. 10). We choose the local calibration because it yields a late Holocene $[PO_4^{3-}]$ estimation of 2.23 µmol/kg that is consistent with the modern hydrographic data. Combining uncertainties of D_{Cd}, RMSE of the Cd_w-$[PO_4^{3-}]$ relation, Cd/Ca measurements, and the age model using the Monte-Carlo approach similar to that used for $[CO_3^{2-}]$ reconstructions, the average uncertainty of our $[PO_4^{3-}]$ reconstructions is ±0.11 µmol/kg (±1σ). Due to the relatively long phosphorus residence time in the ocean (~20–100 ka)[69], we assume little change in the global oceanic $[PO_4^{3-}]$ inventory during the last deglaciation.

Past bottom water $[O_2]$ is estimated from the $\delta^{13}C$ gradient ($\Delta\delta^{13}C$) between epifaunal species *C. wuellerstorfi* and deep infaunal species *G. affinis* using the following equation[27]:

$$\Delta\delta^{13}C = 0.0077^{*}[O_2] + 0.41. \tag{5}$$

The total uncertainty of the $[O_2]$ reconstruction is ±17 µmol/kg (±1σ), which includes both calibration and $\delta^{13}C$ analytical errors[27].

Calculating quasi-conservative tracers

Deep-water PO_4^* is derived from in-situ $[O_2]$ and $[PO_4^{3-}]$ based on the following equation[16,17]:

$$PO_4^* = [PO_4^{3-}] + [O_2]/175 - 1.95. \tag{6}$$

The average ±1σ uncertainty in PO_4^* is 0.15 µmol/kg, derived from errors in $[PO_4^{3-}]$, $[O_2]$, and chronology using an iterated LOESS smoothing method. By definition[16,17], calculation of PO_4^* employs a $R_{-O_2:P}$ value of 175. Using other $R_{-O_2:P}$ values (e.g., 160 or 180) to calculate PO_4^* changes absolute PO_4^* values, but with little effect on its deglacial structure (Supplementary Fig. 6). By definition and due to its conservativeness in the ocean, deep-water PO_4^* incorporates preformed $[PO_4^{3-}]$ and preformed $[O_2]$, that is,

$$PO_4^* = [PO_4^{3-}]_{pre} + [O_2]_{pre}/175 - 1.95. \tag{7}$$

Thus, their relative changes are linked by the following equation:

$$\Delta PO_4^* = \Delta[PO_4^{3-}]_{pre} + \Delta[O_2]_{pre}/175. \tag{8}$$

Following ref. 38, $\Delta[O_2]_{pre}$ can be further divided into two components related to physical and biological changes:

$$\Delta[O_2]_{pre} = \Delta[O_2]_{pre}^{phy} + \Delta[O_2]_{pre}^{bio}. \tag{9}$$

$\Delta[O_2]_{pre}^{phy}$ is determined by surface O_2 solubility, mainly driven by temperature and air-sea gas exchange disequilibrium not related to biological nutrient utilization.

Calculation of $[CO_3^{2-}]_{as}$ is based on the carbonate system sensitivities to changes in physical conditions, remineralization of biogenic organic matter and $CaCO_3$, and air-sea CO_2 gas exchanges, which are derived from hydrographic data in the preindustrial ocean[19]. The carbonate system sensitivities are shown to be similar in preindustrial and LGM conditions[19]. We calculate deglacial $[CO_3^{2-}]_{as}$ changes at site MD97-2106 in four steps following refs. 19,20. In step 1, downcore deep-water $[CO_3^{2-}]$ is normalized to a reference condition (T = 3 °C, S = 35, P = 2500 dbar), using $[CO_3^{2-}]$-T-S-P sensitivities from ref. 19. At site MD97-2106, we estimate deglacial changes in salinity based on global sea level changes, temperature based on benthic foraminiferal $\delta^{18}O$, and water depth based on global sea level changes, following methods described in ref. 19. In step 2, seawater $[CO_3^{2-}]$ changes linked to within-ocean DIC-alkalinity redistributions are calculated by changing in-situ $[PO_4^{3-}]$ to the global average of 2.22 µmol/kg, following the sensitivity of $[CO_3^{2-}]$ change to $[PO_4^{3-}]$ constrained in ref. 19. $[CO_3^{2-}]$ changes are driven by DIC and alkalinity changes related to $[PO_4^{3-}]$ via Redfield Ratio ($R_{C:P} = 127$) and rain ratio (the ratio between organic and inorganic carbon in remineralized biogenic matter, $C_{org}:C_{CaCO_3} = 4$). Using sensitivities of $[CO_3^{2-}]$ change to $[PO_4^{3-}]$ defined by different $R_{C:P}$ and $C_{org}:C_{CaCO_3}$ minimally affects deglacial patterns of $[CO_3^{2-}]_{as}$ (Supplementary Fig. 5). In step 3, deep-water $[CO_3^{2-}]$ changes linked to the global ocean DIC and alkalinity inventory changes due to $CaCO_3$ input/output imbalance over time is calculated following refs. 19,20. Global DIC changes associated with this process are half of the global alkalinity changes, which are the offsets between in-situ alkalinity estimated from model simulations[31] and a reference alkalinity of 2385 µmol/kg. Effects of global DIC-alkalinity changes on $[CO_3^{2-}]$ are derived using the sensitivity of $[CO_3^{2-}]$ to DIC constrained in ref. 19. $CaCO_3$ input/output imbalance mainly contributes to long-term $[CO_3^{2-}]_{as}$ changes. Choosing different modelled deglacial global alkalinity changes leads to varying magnitudes of deglacial $[CO_3^{2-}]_{as}$ changes but minimally affects millennial-timescale structure of $[CO_3^{2-}]_{as}$, as shown by sensitivity tests employing different modelled global alkalinity changes (Supplementary Fig. 5). In step 4, $[CO_3^{2-}]$ changes calculated in Steps 2 and 3 are removed from the $[CO_3^{2-}]$ normailized to a reference condition in Step 1 to obtain the corrected $[CO_3^{2-}]$, whose variabilities are attributed to air-sea CO_2 exchange effects. To derive $[CO_3^{2-}]_{as}$, a constant of 78 µmol/kg is deducted from the corrected $[CO_3^{2-}]$. Deducting this constant brings the late Holocene $[CO_3^{2-}]_{as}$ values close to 0 µmol/kg, which are similar to hydrographic results in the pre-industrial ocean (Figs. 1, 3).

The uncertainty of $[CO_3^{2-}]_{as}$ is also derived using the Monte-Carlo approach. Each $[CO_3^{2-}]_{as}$ was calculated 10,000 times following the abovementioned methods using $[CO_3^{2-}]$, $[PO_4^{3-}]$, temperature, salinity, pressure, and age randomly generated from their averages and standard deviations. The combined ±1σ uncertainty of $[CO_3^{2-}]_{as}$ is derived from the 16th and 84th percentiles of the iterated LOESS-smoothed curves, and our calculation yields an average 1σ-uncertainty of 7.7 µmol/kg for $[CO_3^{2-}]_{as}$.

To reliably infer millennial-timescale changes in PO_4^* and $[CO_3^{2-}]_{as}$, which are derived by combining different proxies, changes in these proxies underlying the preformed tracers need to be synchronized on the same timescale. To ensure synchroneity of these proxies, only reconstructions of $[PO_4^{3-}]$, $[CO_3^{2-}]$, and $[O_2]$, derived from different foraminifera found at the same sediment horizons were combined to calculate PO_4^* and $[CO_3^{2-}]_{as}$. Although the benthic foraminifera that we utilized dwell at varying depths within sediments, they were homogenized by bioturbation within sediments after deposition. This is evident by similar deglacial structures of oxygen isotopes in epifaunal and deep infaunal species in our core (Supplementary Fig. 2). Meanwhile, bioturbation does not prevent millennial-timescale deglacial changes being resolved, due to relatively high sediment rates (15 cm/ka) at our site during the last deglaciation. Finally, from the perspective of tracer calculation, millennial-timescale changes in PO_4^* and $[CO_3^{2-}]_{as}$ are mainly driven by $[O_2]$ and $[CO_3^{2-}]$ with a minor contribution from $[PO_4^{3-}]$ (Fig. 3). For example, the concomitant increases in PO_4^* and $[CO_3^{2-}]_{as}$ during the early HS1 are independent of $[PO_4^{3-}]$ changes.

Calculation of SSW endmember values and sensitivity test

We follow ref. 23 to select hydrographic data (GLODAPv2 dataset)[61,62] to derive NSW and SSW endmember values in the preindustrial ocean. The NSW properties are derived from the North Atlantic sites north of 50°N and deeper than 1500 m, with CFC-11 concentrations >0.5 pmol/kg. The SSW properties are derived from the Southern Ocean sites south of 45°S, and deeper than 1500 m, with CFC-11 concentrations >0.5 pmol/kg and neutral density higher than 28.3 kg/m³ (Supplementary Fig. 1). Following these selection criteria, SSWs defined here are mainly ventilated in the PAZ and reside at deep (~>1500 m) depths in the Pacific Basin. A minor component of SSWs at deep depths is ventilated via the Subantarctic Zone[70], but its contribution during the last deglaciation is smaller than the late Holocene (LH) due to the shallower upper-cell overturning circulation[34], and hence considered to be negligible here.

$PO_4{}^*$ and $[CO_3{}^{2-}]_{as}$ levels during the LH, reconstructed from the top part of core MD97-2106, are consistent with estimations based on preindustrial hydrographic data. As both $PO_4{}^*$ and $[CO_3{}^{2-}]_{as}$ are quasi-conservative, LH $PO_4{}^*$ and $[CO_3{}^{2-}]_{as}$ at site MD97-2106 are determined by linear mixing between NSW and SSW endmembers based on the following equations:

$$PO_4{}^*\_LH^{MD97-2106} = NSW\% \times PO_4{}^*\_LH^{NSW} + SSW\% \times PO_4{}^*\_LH^{SSW} \tag{10}$$

$$[CO_3{}^{2-}]_{as\_LH}{}^{MD97-2106} = NSW\% \times [CO_3{}^{2-}]_{as\_LH}{}^{NSW} + SSW\% \times [CO_3{}^{2-}]_{as\_LH}{}^{SSW} \tag{11}$$

$$NSW\% + SSW\% = 1 \tag{12}$$

Similarly, for the LGM, we have:

$$PO_4{}^*\_LGM^{MD97-2106} = gNSW\% \times PO_4{}^*\_LGM^{NSW} + gSSW\% \times PO_4{}^*\_LGM^{SSW} \tag{13}$$

$$[CO_3{}^{2-}]_{as\_LGM}{}^{MD97-2106} = gNSW\% \times [CO_3{}^{2-}]_{as\_LGM}{}^{NSW} + gSSW\% \times [CO_3{}^{2-}]_{as\_LGM}{}^{SSW} \tag{14}$$

$$gNSW\% + gSSW\% = 1 \tag{15}$$

Equations (13)-(15) can be used to derive $PO_4{}^*{}_{\_LGM}{}^{SSW}$ and $[CO_3{}^{2-}]_{as\_LGM}{}^{SSW}$ from $PO_4{}^*{}_{\_LGM}{}^{MD97\text{-}2106}$ and $[CO_3{}^{2-}]_{as\_LGM}{}^{MD97\text{-}2106}$, if NSW-SSW mixing ratio and NSW endmembers during the LGM are known. The LGM water mass mixing and NSW endmember values are either not firmly quantified or associated with some uncertainties, but their influences on the LGM SSW endmember estimations can be quantified by sensitivity tests.

Based on paleo circulation reconstructions, SSW% in the deep South Pacific was higher during the LGM than the LH[32,33]. We therefore use 80% for the LGM SSW%, compared to 70% for the LH. For $PO_4{}^*$, there currently lacks coupled $[PO_4{}^{3-}]$ and $[O_2]$ reconstructions to constrain $PO_4{}^*{}_{\_LGM}{}^{NSW}$. $[PO_4{}^{3-}]$ reconstructions show that LGM NSW was slightly more nutrient depleted than the modern ocean[19,20,66], while the only published LGM reconstruction suggests similar NSW $[O_2]$ during the LGM and the LH[71]. We thus assume $PO_4{}^*{}_{\_LGM}{}^{NSW}$ to be 80% of the LH level following ref. 37 for our preferred calculations (Table 1), and use $PO_4{}^*{}_{\_LGM}{}^{NSW}$ the same as the LH level for sensitivity tests. We adopt LGM $[CO_3{}^{2-}]_{as}$ reconstructed at a North Atlantic site NEAP4K (61.5°N, 24°W, 1.6 km) as the $[CO_3{}^{2-}]_{as\_LGM}{}^{NSW}$ (-43 ± 5 μmol/kg)[20]. However, glacial deep waters at this site may contain a small fraction of SSWs during the LGM due to the shoaling of NSWs[66]. We thus use $[CO_3{}^{2-}]_{as\_LGM}{}^{NSW}$ derived from 90% NSWs and 10% SSWs at site NEAP4K for sensitivity tests. $[CO_3{}^{2-}]_{as\_LGM}{}^{NSW}$ can be solved from $[CO_3{}^{2-}]_{as\_LGM}$ at sites NEAP4K and MD97-2106, with assumed SSW-NSW mixing ratios at both sites. As shown in Supplementary Fig. 8, our calculated LGM SSW $PO_4{}^*$ and $[CO_3{}^{2-}]_{as}$ employing different SSW% at our site and different NSW endmember levels are well within the ±1σ uncertainties associated with tracer reconstructions, supporting the robustness of our estimates of the LGM SSW endmembers.

Data availability

All new data generated in this study are included in Supplementary Data 1 and have been deposited in the Zenodo data depository at https://doi.org/10.5281/zenodo.14897612.

References

1. Lüthi, D. et al. High-resolution carbon dioxide concentration record 650,000–800,000 years before present. *Nature* **453**, 379–382 (2008).
2. Marcott, S. A. et al. Centennial-scale changes in the global carbon cycle during the last deglaciation. *Nature* **514**, 616–619 (2014).
3. Petit, J.-R. et al. Climate and atmospheric history of the past 420,000 years from the Vostok ice core, Antarctica. *Nature* **399**, 429–436 (1999).
4. Sigman, D. M. & Boyle, E. A. Glacial/interglacial variations in atmospheric carbon dioxide. *Nature* **407**, 859–869 (2000).
5. Sigman, D. M. et al. The southern ocean during the ice ages: a review of the Antarctic surface isolation hypothesis, with comparison to the North Pacific. *Quat. Sci. Rev*. **254**, 106732 (2021).
6. François, R. et al. Contribution of southern ocean surface-water stratification to low atmospheric CO_2 concentrations during the last glacial period. *Nature* **389**, 929–935 (1997).
7. Ito, T. & Follows, M. J. Preformed phosphate, soft tissue pump and atmospheric CO_2. *J. Mar. Res*. **63**, 813–839 (2005).
8. Hain, M. P., Sigman, D. M. & Haug, G. H. Carbon dioxide effects of Antarctic stratification, North Atlantic intermediate water formation, and subantarctic nutrient drawdown during the last ice age: diagnosis and synthesis in a geochemical box model. *Global Biogeochem. Cycles* **24**, 4 (2010).
9. Khatiwala, S., Schmittner, A. & Muglia, J. Air-sea disequilibrium enhances ocean carbon storage during glacial periods. *Sci Adv* **5**, eaaw4981 (2019).
10. Stephens, B. B. & Keeling, R. F. The influence of Antarctic sea ice on glacial–interglacial CO_2 variations. *Nature* **404**, 171–174 (2000).
11. Stein, K., Timmermann, A., Kwon, E. Y. & Friedrich, T. Timing and magnitude of Southern Ocean sea ice/carbon cycle feedbacks. *Proc. Natl Acad. Sci. USA* **117**, 4498–4504 (2020).
12. Marzocchi, A. & Jansen, M. F. Global cooling linked to increased glacial carbon storage via changes in Antarctic sea ice. *Nat. Geosci*. **12**, 1001–1005 (2019).
13. Menviel, L. et al. Southern hemisphere westerlies as a driver of the early deglacial atmospheric CO_2 rise. *Nat. Commun*. **9**, 2503 (2018).
14. Gruber, N., Landschutzer, P. & Lovenduski, N. S. The variable southern ocean carbon sink. *Ann. Rev. Mar. Sci*. **11**, 159–186 (2019).
15. Sigman, D. M., Hain, M. P. & Haug, G. H. The polar ocean and glacial cycles in atmospheric CO_2 concentration. *Nature* **466**, 47–55 (2010).
16. Broecker, W. S., Takahashi, T. & Takahashi, T. Sources and flow patterns of deep-ocean waters as deduced from potential temperature, salinity, and initial phosphate concentration. *J. Geophys. Res*. **90**, 6925 (1985).
17. Broecker, W. S. et al. How much deep water is formed in the southern ocean? *J. Geophys. Res. Oceans* **103**, 15833–15843 (1998).
18. Ito, T., Follows, M. J. & Boyle, E. A. Is AOU a good measure of respiration in the oceans? *Geophys. Res. Lett*. **31**, 17 (2004).
19. Yu, J. et al. More efficient North Atlantic carbon pump during the last glacial maximum. *Nat. Commun*. **10**, 2170 (2019).
20. Yu, J. et al. Millennial and centennial CO_2 release from the southern Ocean during the last deglaciation. *Nat. Geosci*. **15**, 293–299 (2022).
21. Gruber, N., Sarmiento, J. L. & Stocker, T. F. An improved method for detecting anthropogenic CO_2 in the oceans. *Global Biogeochem. Cycles* **10**, 809–837 (1996).
22. Gruber, N. et al. Oceanic sources, sinks, and transport of atmospheric CO_2. *Global Biogeochem. Cycles* **23**, 1 (2009).

23. Rae, J. W. B. & Broecker, W. What fraction of the Pacific and Indian oceans' deep water is formed in the southern ocean? *Biogeosciences* **15**, 3779–3794 (2018).
24. Yu, J. & Elderfield, H. Benthic foraminiferal B/Ca ratios reflect deep water carbonate saturation state. *Earth Planet. Sci. Lett.* **258**, 73–86 (2007).
25. Boyle, E. A., Labeyrie, L. & Duplessly, J. C. Calcitic foraminiferal data confirmed by cadmium in aragonitic *Hoeglundina*: application to the last glacial maximum in the northern indian ocean. *Paleoceanography* **10**, 881–900 (1995).
26. Boyle, E. A. Cadmium and $\delta^{13}C$ paleochemical ocean distributions during the stage 2 glacial maximum. *Annu. Rev. Earth Planetary Sci.* **20**, 245 (1992).
27. Hoogakker, B. A. A., Elderfield, H., Schmiedl, G., McCave, I. N. & Rickaby, R. E. M. Glacial–interglacial changes in bottom-water oxygen content on the Portuguese margin. *Nat. Geosci.* **8**, 40–43 (2014).
28. Dai, Y., Yu, J. & Rafter, P. Deglacial ventilation changes in the deep southwest pacific. *Paleoceanogr. Paleoclimatol.* **36**, e2020PA004172 (2021).
29. Dai, Y., Yu, J., Ren, H. & Ji, X. Deglacial subantarctic CO_2 outgassing driven by a weakened solubility pump. *Nat. Commun.* **13**, 5193 (2022).
30. Gottschalk, J. et al. Glacial heterogeneity in southern ocean carbon storage abated by fast South Indian deglacial carbon release. *Nat. Commun.* **11**, 6192 (2020).
31. Köhler, P. & Munhoven, G. Late pleistocene carbon cycle revisited by considering solid earth processes. *Paleoceanogr. Paleoclimatol.* **35**, e2020PA004020 (2020).
32. Basak, C. et al. Breakup of last glacial deep stratification in the South Pacific. *Science* **359**, 900–904 (2018).
33. Noble, T. L., Piotrowski, A. M. & McCave, I. N. Neodymium isotopic composition of intermediate and deep waters in the glacial southwest Pacific. *Earth Planet. Sci. Lett.* **384**, 27–36 (2013).
34. Ferrari, R. et al. Antarctic sea ice control on ocean circulation in present and glacial climates. *Proc. Natl Acad. Sci. USA* **111**, 8753–8758 (2014).
35. Sikes, E. L., Elmore, A. C., Allen, K. A., Cook, M. S. & Guilderson, T. P. Glacial water mass structure and rapid $\delta^{18}O$ and $\delta^{13}C$ changes during the last glacial termination in the southwest Pacific. *Earth Planet. Sci. Lett.* **456**, 87–97 (2016).
36. Rae, J. W. B. et al. CO_2 storage and release in the deep southern Ocean on millennial to centennial timescales. *Nature* **562**, 569–573 (2018).
37. Vollmer, T. D., Ito, T. & Lynch-Stieglitz, J. Proxy-based preformed phosphate estimates point to increased biological pump efficiency as primary cause of last glacial maximum CO_2 drawdown. *Paleoceanogr. Paleoclimatol.* **37**, e2021PA004339 (2022).
38. Cliff, E., Khatiwala, S. & Schmittner, A. Glacial deep ocean deoxygenation driven by biologically mediated air–sea disequilibrium. *Nat. Geosci.* **14**, 43–50 (2021).
39. Broecker, W. S. & Peng, T. H. Gas exchange rates between air and sea. *Tellus* **26**, 21–35 (1974).
40. Zeebe, R. E. & Wolf-Gladrow, D. *CO_2 in Seawater: Equilibrium, Kinetics, Isotopes: Equilibrium, Kinetics, Isotopes*, Vol. 346 (Elsevier, 2001).
41. Anderson, R. F. et al. Wind-driven upwelling in the southern ocean and the deglacial rise in atmospheirc CO_2. *Science* **323**, 1443–1448 (2009).
42. Wang, X. T. et al. Deep-sea coral evidence for lower southern ocean surface nitrate concentrations during the last ice age. *Proc. Natl Acad. Sci. USA* **114**, 3352–3357 (2017).
43. Li, T. et al. Rapid shifts in circulation and biogeochemistry of the southern ocean during deglacial carbon cycle events. *Sci. Adv.* **6**, eabb3807 (2020).
44. Ai, X. E. et al. Southern Ocean upwelling, Earth's obliquity, and glacial-interglacial atmospheric CO_2 change. *Science* **370**, 1348–1352 (2020).
45. Studer, A. S. et al. Antarctic zone nutrient conditions during the last two glacial cycles. *Paleoceanography* **30**, 845–862 (2015).
46. Members, W. D. P. Onset of deglacial warming in west Antarctica driven by local orbital forcing. *Nature* **500**, 440–444 (2013).
47. Gray, W. R. et al. Poleward shift in the southern hemisphere westerly winds synchronous with the deglacial rise in CO_2. *Paleoceanogr. Paleoclimatol.* **38**, e2023PA004666 (2023).
48. McManus, J., Francois, R., Gherardi, J. M., Keigwin, L. & Brown-Leger, S. Collapse and rapid resumption of Atlantic meridional circulation linked to deglacial climate changes. *Nature* **428**, 834–837 (2004).
49. Lynch-Stieglitz, J. et al. A diminished north Atlantic nutrient stream during younger dryas climate reversal. *Science* **384**, 693–696 (2024).
50. Skinner, L. C., Fallon, S., Waelbroeck, C., Michel, E. & Barker, S. Ventilation of the deep southern ocean and deglacial CO_2 rise. *Science* **328**, 1147–1151 (2010).
51. Muglia, J. & Schmittner, A. Carbon isotope constraints on glacial Atlantic meridional overturning: strength vs depth. *Quat. Sci. Rev.* **257**, 106844 (2021).
52. Stewart, J. A. et al. Arctic and Antarctic forcing of ocean interior warming during the last deglaciation. *Sci. Rep.* **13**, 22410 (2023).
53. Stewart, J. A. et al. Productivity and dissolved oxygen controls on the southern ocean deep-sea benthos during the Antarctic cold reversal. *Paleoceanogr. Paleoclimatol.* **36**, e2021PA004288 (2021).
54. Fogwill, C. J. et al. Southern ocean carbon sink enhanced by sea-ice feedbacks at the Antarctic cold reversal. *Nat. Geosci.* **13**, 489–497 (2020).
55. Yu, J. et al. Millennial atmospheric CO_2 changes linked to ocean ventilation modes over past 150,000 years. *Nat. Geosci.* **16**, 1166–1173 (2023).
56. Rae, J. W. B., Foster, G. L., Schmidt, D. N. & Elliott, T. Boron isotopes and B/Ca in benthic foraminifera: proxies for the deep ocean carbonate system. *Earth Planet. Sci. Lett.* **302**, 403–413 (2011).
57. Barker, S., Greaves, M. & Elderfield, H. A study of cleaning procedures used for foraminiferal Mg/Ca paleothermometry. *Geochem. Geophys. Geosyst.* (2003).
58. Yu, J., Elderfield, H., Greaves, M. & Day, J. Preferential dissolution of benthic foraminiferal calcite during laboratory reductive cleaning. *Geochem. Geophys. Geosyst.* **8**, Q06016 (2007).
59. Boyle, E. & Keigwin, L. Comparison of Atlantic and Pacific paleochemical records for the last 215,000 years: changes in deep ocean circulation and chemical inventories. *Earth Planet. Sci. Lett.* **76**, 135–150 (1985).
60. Yu, J., Day, J., Greaves, M. & Elderfield, H. Determination of multiple element/calcium ratios in foraminiferal calcite by quadrupole ICP-MS. *Geochem. Geophys. Geosyst.* **6**, Q08P01 (2005).
61. Lauvset, S. K. et al. A new global interior ocean mapped climatology: the 1° × 1° GLODAP version 2. *Earth Syst. Sci. Data* **8**, 325–340 (2016).
62. Olsen, A. et al. GLODAPv2.2019 – an update of GLODAPv2. *Earth Syst. Sci. Data* **11**, 1437–1461 (2019).
63. Lewis, E., Wallace, D. & Allison, L. J. *Program Developed for CO_2 System Calculations*. (Carbon Dioxide Information Analysis Center, managed by Lockheed Martin Energy Research Corporation for the US Department of Energy Tennessee, 1998).
64. Yu, J. et al. Responses of the deep ocean carbonate system to carbon reorganization during the last glacial–interglacial cycle. *Quat. Sci. Rev.* **76**, 39–52 (2013).
65. Boyle, E. A. Cadmium: Chemical tracer of deepwater paleoceanography. *Paleoceanography* **3**, 471–489 (1988).

66. Marchitto, T. M. & Broecker, W. S. Deep water mass geometry in the glacial Atlantic ocean: a review of constraints from the paleonutrient proxy Cd/Ca. *Geochem. Geophys. Geosyst.* **7,** 12 (2006).
67. Schlitzer, R. et al. The GEOTRACES intermediate data product 2017. *Chem. Geol.* **493**, 210–223 (2018).
68. GEOTRACES Intermediate Data Product Group. *The GEOTRACES Intermediate Data Product 2021 version 2 (IDP2021v2)*. https://www.bodc.ac.uk/data/published_data_library/catalogue/10.5285/ff46f034-f47c-05f9-e053-6c86abc0dc7e/ (2023).
69. Broecker, W. S., Peng, T.-H. & Beng, Z. *Tracers in the Sea*, Vol 690 (Lamont-Doherty Geological Observatory, Columbia University, 1982).
70. Gebbie, G. & Huybers, P. Total matrix intercomparison: a method for determining the geometry of water-mass pathways. *J. Phys. Oceanogr.* **40**, 1710–1728 (2010).
71. Mojtahid, M. et al. Changes in northeast Atlantic hydrology during termination 1: insights from celtic margin's benthic foraminifera. *Quat. Sci. Rev.* **175**, 45–59 (2017).
72. Members, E. C. Eight glacial cycles from an Antarctic ice core. *Nature* **429**, 623–628 (2004).
73. Andersen, K. K. et al. High-resolution record of northern Hemisphere climate extending into the last interglacial period. *Nature* **431**, 147–151 (2004).

Acknowledgements

J.Y. acknowledges support from NSF China 42330403. Y.D. acknowledges support from the Australian Research Council Special Research Initiative, Australian Centre for Excellence in Antarctic Science (Project Number SR200100008). We thank Brad Opdyke for assistance with sediment sampling.

Author contributions

J.Y. designed the project. Y.D. wrote the first draft of the manuscript with significant inputs from J.Y. Y.D. made geochemical measurements and performed data analyses and visualization. Both authors contributed to the interpretation of the data and refinement of the manuscript.

Competing interests

The authors declare no competing interests.

Additional information

Supplementary information The online version contains supplementary material available at https://doi.org/10.1038/s41467-025-57677-x.

Correspondence and requests for materials should be addressed to Yuhao Dai or Jimin Yu.

Peer review information *Nature Communications* thanks Jesse Farmer and the other, anonymous, reviewer(s) for their contribution to the peer review of this work. A peer review file is available.

Reprints and permissions information is available at http://www.nature.com/reprints